

Designing Thermoplasmonic Properties of Metallic Metasurfaces

Ch. Girard, P. R. Wiecha, A. Cuche, and E. Dujardin

CEMES, University of Toulouse and CNRS (UPR 8011), 29 rue Jeanne Marvig, BP 94347, 31055 Toulouse, France

Abstract. Surface plasmons have been used recently to generate heat nanosources, the intensity of which can be tuned, for example, with the wavelength of the excitation radiation. In this paper, we present versatile analytical and numerical investigations for the three-dimensional computation of the temperature rise in complex planar arrays of metallic particles. In the particular case of elongated particles sustaining transverse and longitudinal plasmon modes, we show a simple temperature rise control of the surrounding medium when turning the incident polarization. This formalism is then used for designing novel thermoplasmonic metasurfaces for the nanoscale remote control of heat flux and temperature gradients.

PACS numbers: 41.20.-q, 78.20.Bh, 73.20.Mf

1. Introduction

The ability of metal structures to confine the electromagnetic fields gave birth to a multitude of applications in areas as diverse as biophysics, sensor technology or devices for fast data processing[1, 2, 3]. The light confinement phenomenon originates in the surface plasmons (SP) travelling or localized at the surface of these nanostructures. Most plasmonics applications, based on the engineering of surface plasmons, exploit the electromagnetic fields produced by the collective electronic oscillations. In particular, SP engineering has been considered as a viable approach to the coplanar implementation of high speed, low dissipative information devices using analogical or digital concepts[4, 5]. Very recently, plasmonics has fostered another realm of applications in which dissipative effects are being advantageously utilized [6, 7, 8, 9, 10, 11, 12, 13, 14, 15]. Indeed, besides their widely used propensity to enhance and confine the near-field electromagnetic intensity, metal particles and nanostructures have revealed a great potential as local heat sources[6, 7, 11, 16]. A realistic description of such localized dissipation effects is directly related to the description of the imaginary part of the dynamical response functions of the nanostructures, such as the dielectric permittivity of the metal $\epsilon(\omega)$, and the local electric field intensity $I_l(\mathbf{r}, \omega)$ induced inside the metal[7, 11, 17, 18]. While the dielectric constant only depends on the nature of the metal, the intensity distribution of the optical electric field induced in the particle is extremely sensitive to the presence of plasmon resonances occurring in the spectral variation of the local field distribution $I_l(\mathbf{r}, \omega)$ [7, 17, 19, 20]. These resonances play a crucial role since the amount of heat transferred to the particle can be adjusted by tuning the incident wavelength in or out of the resonance range. Several experimental thermoplasmonic building blocks have indeed been designed from this concept and realized from colloidal chemistry or sophisticated lithography processes [13, 14, 16, 21].

In this paper, we propose a flexible analytical scheme [22, 23] completed by numerical studies [19] to investigate the thermoplasmonic properties of arrays of individual plasmonic entities with arbitrary shapes sustaining multiple plasmon modes in the optical range. Arrays of nanostructures are systems of fundamental interest in plasmonics since they combine the optical properties of individual resonators and the collective response of the assembly. Such systems have already contributed to major breakthroughs in several fields in optics like optical sensing, metasurfaces for light phase and orbital angular momentum control, strong optical coupling, ... [24, 25, 26, 27]. In a typical configuration, the particle arrangement is supported by a planar dielectric substrate. Here we apply the well-established self-consistent scheme based on the Green Dyadic Functions (GDF) formalism and compute the local field intensity inside the particle array by including the coupling with the substrate. The average temperature in the vicinity of the metallic structures is then derived from the local field intensity.

As a first step towards realistic configurations, we describe each individual metal structure as an anisotropic polarizable particle excited by their self-consistent local electric field[28]. This first approach consists in gradually developing a quasi-analytical

description of the calculation that provides an intuitive access to the underlying physical and thermal mechanisms. This simple analytical description is then complemented by an adequate discretisation of the particle physical volumes in order to describe arbitrary geometries[19]. The numerical applications are based on the permittivity of gold taken from Johnson and Christy data[29]. In the third section, the specific case of periodic arrays of gold nanorods is investigated and we demonstrate a simple and reversible control of the temperature rise near the particles when turning the incident polarization. Applications to the new concept of thermoplasmonic metasurfaces are then discussed in the two last sections where we demonstrate that our numerical technique is well-suited for the design of optimized thermoplasmonic meta-cells, using an evolutionary optimization (EO) algorithm.

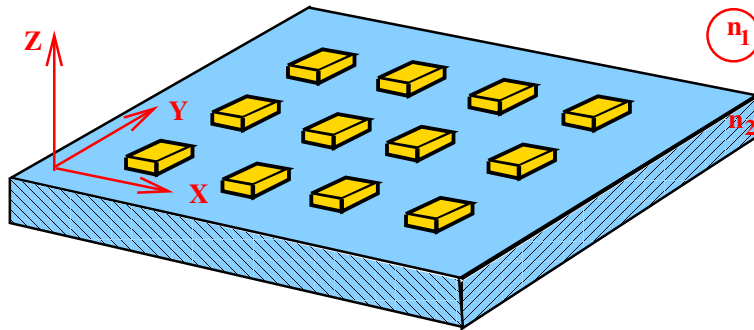


Figure 1. (color online) Perspective view illustrating a periodic assembly of plasmonic structures fabricated at the surface of an insulating sample.

2. Thermal response of a periodic array of identical metal particles

Let us consider a periodic 2D array of N elongated gold structures arranged in a periodic way at the surface of a dielectric planar substrate (Fig. (1)). The particle location is defined by a set of N vectors $\mathbf{r}_i = (\mathbf{L}_i, Z)$ (where the two-dimensional vector \mathbf{L}_i belongs to the (XOY) plane). Unlike what happens with perfectly spherical particles, single nanorods exhibit extinction spectra with two plasmon bands that correspond to electron oscillations along their length (low energy longitudinal mode) and across their section (high energy transverse mode) [30]. This shape effect can be described with a simple analytical model by using an anisotropic dynamical polarisability [28]. When the long axis of the particles is aligned along (OY) axis as shown in figure (1), the polarizability tensor is diagonal and reads:

$$\alpha(\omega_0) = \begin{pmatrix} \alpha_{\perp}(\omega_0) & 0 & 0 \\ 0 & \alpha_{\parallel}(\omega_0) & 0 \\ 0 & 0 & \alpha_{\perp}(\omega_0) \end{pmatrix}, \quad (1)$$

where the two independent components $\alpha_{\perp}(\omega_0)$ and $\alpha_{\parallel}(\omega_0)$ can be described by the formula associated with a prolate ellipsoid [28].

2.1. Local field calculation

When a monochromatic electromagnetic plane wave of frequency ω_0 and electric field amplitude \mathbf{E}_0 hits the interface between environment (media 1) and the glass substrate (media 2) at normal incidence and interacts with the metallic particles, the optical electric field can be written:

$$\mathbf{E}_0(\mathbf{r}, t) = \frac{1}{2} \{ \mathbf{E}_0(\mathbf{r}, \omega_0) \exp(i\omega_0 t) + C.C. \} , \quad (2)$$

where $\mathbf{E}_0(\mathbf{r}, \omega_0)$ (with $\mathbf{r} = (x, y, z)$) represents its Fourier amplitude:

$$\mathbf{E}_0(\mathbf{r}, \omega_0) = \mathbf{E}_0[\exp(-in_1 k_0 z) + R \exp(in_1 k_0 z)] , \quad (3)$$

in which k_0 is the wave vector modulus in vacuum and $R = (n_1 - n_2)/(n_1 + n_2)$ is the Fresnel reflection coefficient expressed with the optical indices of surrounding medium (n_1) and dielectric substrate (n_2), respectively. The polarization of the incident wave, associated with the direction of the vector \mathbf{E}_0 , can be materialized by the angle θ between \mathbf{E}_0 and the (OX) axis:

$$\mathbf{E}_0 = E_0(\cos(\theta), \sin(\theta), 0) . \quad (4)$$

2.1.1. Self-consistency The local fields $\mathbf{E}(\mathbf{r}_i, \omega_0)$ induced at the center of the particles by the illumination field verify a set of N coupled equations that can be condensed as follows:

$$\mathcal{E}_0(\omega_0) = \mathcal{M}(\omega_0) \cdot \mathcal{E}(\omega_0) \quad (5)$$

where $\mathcal{E}_0(\omega_0)$ is the *input* supervector that contains the N incident fields at the particle locations:

$$\mathcal{E}_0(\omega_0) = \{ \mathbf{E}_0(\mathbf{r}_1, \omega_0), \dots, \mathbf{E}_0(\mathbf{r}_i, \omega_0), \dots \} , \quad (6)$$

and $\mathcal{E}(\omega_0)$ is the *output* supervector that contains the local field values:

$$\mathcal{E}(\omega_0) = \{ \mathbf{E}(\mathbf{r}_1, \omega_0), \dots, \mathbf{E}(\mathbf{r}_i, \omega_0), \dots \} . \quad (7)$$

For N polarizable particles, the $(3N \times 3N)$ coupling matrix $\mathcal{M}(\omega_0)$ has a very simple form given by:

$$\mathcal{M}(\omega_0) = \mathcal{I} - \mathcal{A}(\omega_0) , \quad (8)$$

where \mathcal{I} is the identity matrix and:

$$\mathcal{A}(\omega_0) = \begin{pmatrix} \mathbf{A}_{11}(\omega_0) & \dots & \mathbf{A}_{1j}(\omega_0) & \dots \\ \dots & \dots & \dots & \dots \\ \dots & \mathbf{A}_{ij}(\omega_0) & \dots & \dots \\ \dots & \dots & \dots & \mathbf{A}_{NN}(\omega_0) \end{pmatrix} , \quad (9)$$

is composed of N^2 submatrices defined from the particle polarizabilities and the field-propagators $\mathbf{S}(\mathbf{r}_i, \mathbf{r}_j, \omega_0)$ between two particles locations, \mathbf{r}_i and \mathbf{r}_j :

$$\mathbf{A}_{ij}(\omega_0) = \mathbf{S}(\mathbf{r}_i, \mathbf{r}_j, \omega_0) \cdot \alpha(\omega_0) \quad (10)$$

2.1.2. *Weak coupling between individual metallic nanostructures* The calculation of the local field in the particle array needs the inversion of the matrix $\mathcal{M}(\omega_0)$ shown by equation (5), which can be considerably simplified depending on the interparticle spacing D . For example, when the lateral spacing D is of the order of the incident wavelength λ_0 and the thickness of the metal particles is much smaller, the mutual interactions vanish so that all the tensorial components $\mathbf{S}(\mathbf{r}_i, \mathbf{r}_j, \omega_0) \cdot \alpha(\omega_0) \ll 1$. This hypothesis, that corresponds to the first Born approximation (FBA), leads to the simplified relation:

$$\mathcal{M}^{-1}(\omega_0) = \mathcal{I} + \mathcal{A}(\omega_0) + O(\mathcal{A}^2), \quad (11)$$

2.2. Dissipated power

During the illumination process, the temperature rises because of the electronic Joule effect induced inside the metal particles. This dissipative energy channel can be described by computing the power per unit volume dissipated inside the metal. From the electric field $\mathbf{E}_i(\mathbf{r}, t)$ and the induction vector $\mathbf{D}_i(\mathbf{r}, t)$, we can derive the amount of power dissipated by the i^{th} metallic particle. In CGS electrostatic units, this leads to:

$$\mathcal{Q}(\mathbf{r}_i) = \frac{1}{4\pi} \int_{v_i} d\mathbf{r} \langle \mathbf{E}_i(\mathbf{r}, t) \cdot \frac{\partial}{\partial t} \mathbf{D}_i(\mathbf{r}, t) \rangle, \quad (12)$$

where the integral runs over the particle volume, and the brackets schematize the time average. Similarly to equation (2), the vectors $\mathbf{E}_i(\mathbf{r}, t)$ and $\mathbf{D}_i(\mathbf{r}, t)$ can be expressed in term of their Fourier amplitudes $\mathbf{E}_i(\mathbf{r}, \omega_0)$ and $\mathbf{D}_i(\mathbf{r}, \omega_0)$. After taking the time average, this transformation leads to:

$$\begin{aligned} \mathcal{Q}(\mathbf{r}_i) = & \frac{1}{16\pi} \int_{v_i} i\omega_0 \left\{ \mathbf{E}_i(\mathbf{r}, \omega_0) \cdot \mathbf{D}_i^*(\mathbf{r}, \omega_0) \right. \\ & \left. - \mathbf{E}_i^*(\mathbf{r}, \omega_0) \cdot \mathbf{D}_i(\mathbf{r}, \omega_0) \right\} d\mathbf{r}, \end{aligned} \quad (13)$$

Next, we introduce the constitutive relation between $\mathbf{D}_i(\mathbf{r}, \omega_0)$ and $\mathbf{E}_i(\mathbf{r}, \omega_0)$. Rewriting this equation in a tensorial form will allow to consider non-spherical particles:

$$\mathbf{D}_{i,\alpha}(\mathbf{r}, \omega_0) = \sum_{\beta} \epsilon_{\alpha,\beta}(\omega_0) \mathbf{E}_{i,\beta}(\mathbf{r}, \omega_0), \quad (14)$$

where α and β are two cartesian indices. After replacing (14) into (13) and assuming a diagonal form for $\epsilon_{\alpha,\beta}(\omega_0)$ one gets:

$$\mathcal{Q}(\mathbf{r}_i) = \frac{\omega_0}{8\pi} \int_{v_i} \left\{ \sum_{\alpha} \Im \epsilon_{\alpha,\alpha}(\omega_0) |\mathbf{E}_{i,\alpha}(\mathbf{r}, \omega_0)|^2 \right\} d\mathbf{r}, \quad (15)$$

where the \Im symbol means *imaginary part*. Equation (15) is general and does not contain any approximation and applies to arbitrary geometries and any type of materials.

2.2.1. *Dipolar response approximation* For metallic particles of small size, the multipolar contributions higher than the dipolar one can be neglected. In this case,

the permittivity of the i^{th} particle can be schematized by the following relation in which $\delta(\mathbf{r} - \mathbf{r}_i)$ represents the Dirac δ distribution centered around the particle location \mathbf{r}_i :

$$\epsilon(\omega_0) = 1 + 4\pi \begin{pmatrix} \alpha_{\perp}(\omega_0) & 0 & 0 \\ 0 & \alpha_{\parallel}(\omega_0) & 0 \\ 0 & 0 & \alpha_{\perp}(\omega_0) \end{pmatrix} \times \delta(\mathbf{r} - \mathbf{r}_i). \quad (16)$$

From this simplified relation it is straightforward to perform the volume integral found in equation (15):

$$\begin{aligned} \mathcal{Q}(\mathbf{r}_i) = & \frac{\omega_0}{2} \left\{ \Im \alpha_{\perp}(\omega_0) |\mathbf{E}_{i,y}(\mathbf{r}_i, \omega_0)|^2 \right. \\ & \left. + \Im \alpha_{\parallel}(\omega_0) (|\mathbf{E}_{i,x}(\mathbf{r}_i, \omega_0)|^2 + |\mathbf{E}_{i,z}(\mathbf{r}_i, \omega_0)|^2) \right\}, \end{aligned} \quad (17)$$

Notably, a more accurate calculation of both the local fields and the successive field-gradients would require to go beyond the dipolar approximation. However, the proposed description makes it possible to derive the analytical calculation throughout its development.

2.2.2. The particular case of a single elongated plasmonic particle When the metallic pattern simply consists in a single particle located at the position \mathbf{r}_1 , the collective effects vanish and the matrix $\mathcal{M}^{-1}(\omega_0) = \mathcal{I}$ which means that the local electric field $\mathbf{E}(\mathbf{r}_1, \omega_0) = \mathbf{E}_0(\mathbf{r}_1, \omega_0)$. This asymptotic case gives rise to a particularly simple equation that can be obtained by using Eqs. (3) and (4):

$$\mathcal{Q} = \frac{E_0^2 \omega_0}{2} \left\{ \Im \alpha_{\perp}(\omega_0) \cos^2(\theta) + \Im \alpha_{\parallel}(\omega_0) \sin^2(\theta) \right\}. \quad (18)$$

Here, we explicitly see how tuning the polarization angle θ controls the amount of heat transferred to the particle. Finally, after introducing the well-known relation between electric field amplitude E_0 and laser power S_0 delivered per unit area [31]:

$$E_0^2 = \frac{8\pi S_0}{c}, \quad (19)$$

one obtains:

$$\mathcal{Q} = 4\pi S_0 k_0 \left\{ \Im \alpha_{\perp}(\omega_0) \cos^2(\theta) + \Im \alpha_{\parallel}(\omega_0) \sin^2(\theta) \right\}. \quad (20)$$

In this last equation, the influence of the relative weights of both transverse and longitudinal plasmon modes clearly appears through the two components of the nanorod polarizability. To illustrate how this equation governs the heat absorbed by a single ellipsoidal gold nanorod, we present in Fig (2) a sequence of four maps $\mathcal{Q}(\lambda_0, \theta)$ for aspect ratios $\eta = a/b$ varying from 1 to 4. The laser power S_0 is set at $1 \text{ mW}/\mu\text{m}^2$ and the particle long axis is chosen parallel to the (OY) cartesian axis. In the (λ_0, θ) coordinate plane, the resulting heat response of the particle varies from polarization-independent dissipation maximized at low incident wavelength for the sphere case (characterized by a single color band), to an oblong domain that is shifted to longer incident wavelength as η increases and shows an optimum for 90° polarization angle.

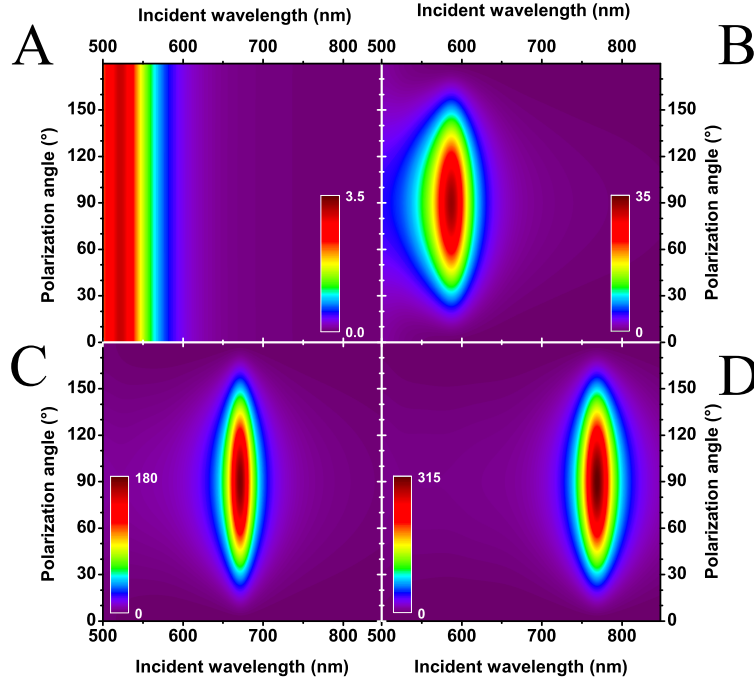


Figure 2. (color online) Simulation of four color plots of the heat $Q(\lambda_0, \theta)$ dissipated per time unit as a function of the incident wavelength ($500 \text{ nm} \leq \lambda_0 \leq 850 \text{ nm}$) and the polarization angle ($0 \leq \theta \leq 180^\circ$) for a gold prolate ellipsoid of short and long axis b and a , respectively. In maps (A) to (D), four aspect ratio $\eta = a/b$ have been considered: (A) sphere case ($\eta = 1$) $a = b = 10 \text{ nm}$; (B) ellipsoid ($\eta = 2$) $a = 20 \text{ nm}$ and $b = 10 \text{ nm}$; (C) ellipsoid ($\eta = 3$) $a = 30 \text{ nm}$ and $b = 10 \text{ nm}$; and (D) ellipsoid ($\eta = 4$) $a = 40 \text{ nm}$ and $b = 10 \text{ nm}$. All the color bars are expressed in nanoWatt (nW).

2.2.3. Volume discretization approach Finding exact solutions of equation (12) for more realistic situations requires an additional volume discretization procedure of the source region occupied by the plasmonic particles. Generally, each particle volume V_p is discretized into n_p identical elementary volumes v_p . Such a procedure converts integrals into discrete summations. The main analytical steps of this technique are detailed in reference[19] and lead to:

$$\begin{aligned} \mathbf{E}(\mathbf{r}_{t,i}, \omega_0) &= \mathbf{E}_0(\mathbf{r}, \omega_0) + \sum_{p=1}^N \chi_p(\omega_0) \sum_{j=1}^{n_p} \\ &\times \mathbf{S}(\mathbf{r}_{t,i}, \mathbf{r}_{p,j}, \omega_0) \cdot \mathbf{E}(\mathbf{r}_{p,j}, \omega_0). \end{aligned} \quad (21)$$

In this expression, the parameters $\chi_p(\omega_0)$ associated with the elementary volumes v_p are homogeneous to dipolar polarizabilities:

$$\chi_p(\omega_0) = \frac{\epsilon_p(\omega_0) - \epsilon_{env}(\omega_0)}{4\pi} v_p. \quad (22)$$

The vectors $\mathbf{r}_{p,j}$ and $\mathbf{r}_{t,i}$ represent the location of j^{th} and i^{th} discretized cells inside the p^{th} and t^{th} metallic particles, respectively. Next, the self-consistent electric field inside the metal particles is computed. This procedure leads to a system of $N \times n_p$ vectorial equations with $N \times n_p$ unknown fields $\mathbf{E}(\mathbf{r}_{p,j}, \omega_0)$.

For a given metal particle (labelled by the subscript p), the solving procedure detailed in reference[19] is directly related to the discretization volume v_p , which itself depends on the discretization grid used to mesh the particles. The expressions of the $\chi_p(\omega_0)$ coefficients for both cubic and hexagonal compact discretization grids can be found in table (1) of reference [19].

3. Temperature Profile

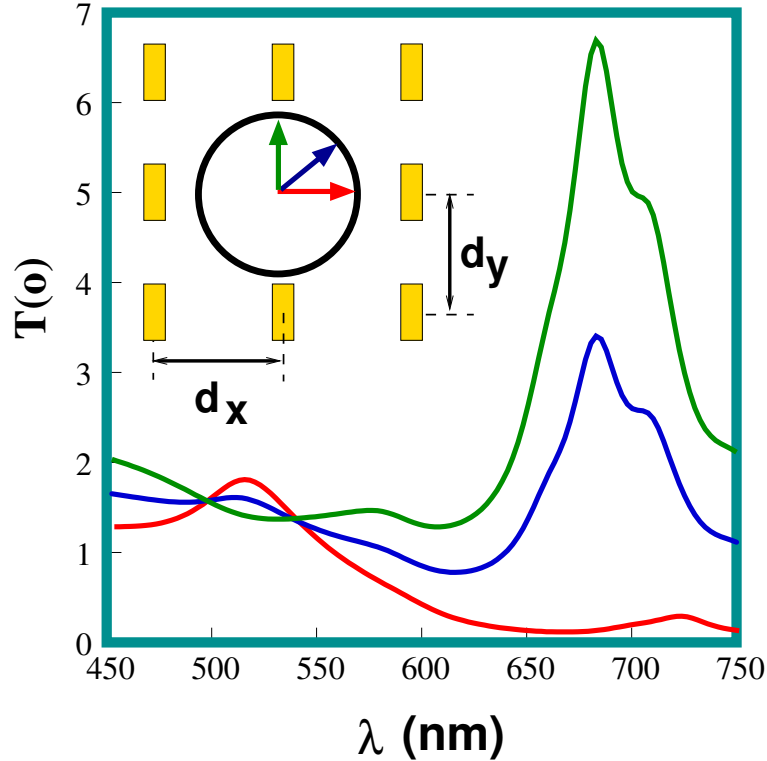


Figure 3. (color online) Simulation of three temperature spectra computed above a set of nine cylindric gold nanorods (25×80 nm) illuminated in normal incidence by a linearly polarized plane wave (see geometry insert). The laser power S_0 is fixed at $5 \text{ mW}/\mu\text{m}^2$ and the lateral pitches, d_x and d_y between the rods is 500 nm. The three spectra correspond to the polarization directions indicated by the red, blue and green arrows. The computation has been performed by discretization of the nanorod volumes by $N \times 333$ elementary cells distributed over a hexagonal compact three-dimensional mesh.

The steady-state temperature increase, $\Delta T(\lambda_0, \theta)$, can be deduced from the distribution of heat $\mathcal{Q}(\mathbf{r}_{p,j})$ deposited inside the particle lattice (cf. Eq. (15)), by the thermal Poisson equation:

$$\Delta T(\lambda_0, \theta) = \frac{1}{4\pi\kappa} \sum_{p=1}^N \sum_{j=1}^{n_p} \frac{\mathcal{Q}(\mathbf{r}_{p,j})}{|\mathbf{R}_{obs} - \mathbf{r}_{p,j}|} \quad (23)$$

where κ is the environmental thermal conductivity and \mathbf{R}_{obs} defines an observation point located in the vicinity of the sample. In figures (3) and (4), we have used relation (23)

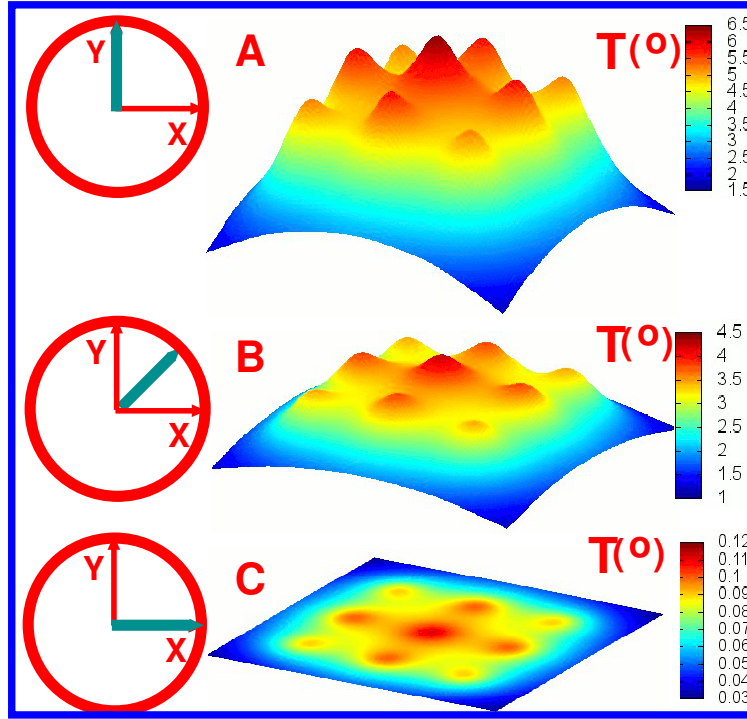


Figure 4. (color online) 3D color plots of three simulations of the temperature distribution above a set of nine gold nanorods corresponding to incident polarization aligned (A) along Y axis, (B) at 45° and (C) along the X axis (same parameters as figure (3)). The wavelength, $\lambda_0 = 680$ nm, is chosen at the center of the longitudinal plasmon band.

to investigate the photothermal effects induced near an array of nine gold nanorods deposited on a dielectric surface (see insert of figure (3)). The metal particles are surrounded by an isotropic medium of refractive index $n_1 = 1.33$, mimicking an aqueous medium.

The spectral variation of the temperature as a function of the incident wavelength is presented in figure (3). The temperature shift $\Delta T(\lambda_0, \theta)$ is computed from equation (23) at a position $\mathbf{R}_{obs} = (0, 0, 150\text{nm})$ which overhangs the central gold pad. The three polarisation directions considered here, *i.e.* zero degree (red curve); 45° (blue curve) and 90° (green curve), demonstrate that the temperature around the metal pattern can be effectively tuned with a drastic increase observed near the longitudinal resonance. Thus, by exciting the longitudinal plasmon band ($\lambda = 680$ nm) of the sample, the local temperature can be modulated over one order of magnitude by the simple tuning of the the field polarization. Obviously, this control is much less effective when exciting the transverse mode ($\lambda = 530$ nm) because of a weaker quality factor. In addition this resonance is bound by two isobestic points [32] at 500 and 540 nm, where the temperature is independent of the polarization (Figure 3).

Finally, figure (4) shows a sequence of three temperature maps resulting from the monochromatic excitation of the longitudinal band ($\lambda = 680$ nm) at normal incidence

with a plane wave. All three maps are displayed with the same vertical scale to highlight the temperature rise occurring when the incident polarization is aligned with the main axis of the nanorods. A general observation is the strong temperature rise in the direct vicinity of individual metallic structures and the broader yet less intense temperature increase over the entire pattern [21].

4. Metasurfaces for Thermoplasmonic control

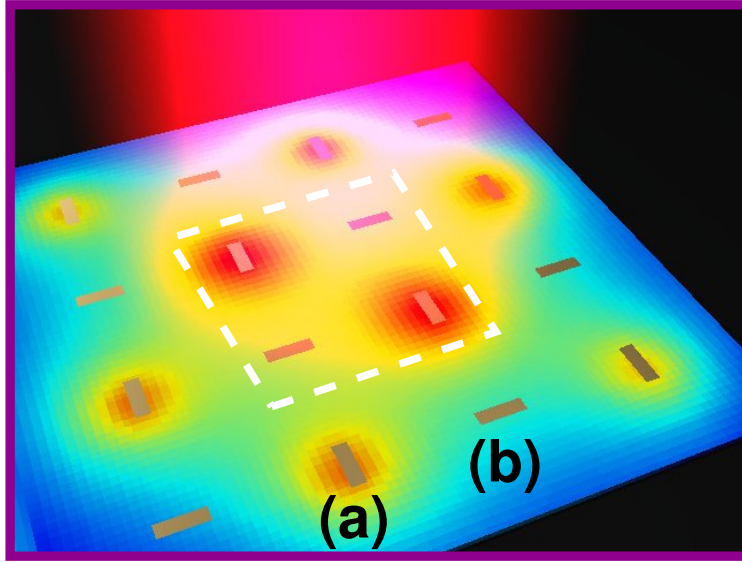


Figure 5. (color online) Example of thermoplasmonic metasurface able to generate strong temperature contrast. The unit cell, located inside the dashed white frame, is a set of four gold nanorods perpendicular to each other. The labels (a) and (b) represents two consecutive rod orientations, parallel and antiparallel, inside the pattern. The metasurface is superimposed by a temperature map computed with a incident polarization aligned along the (a) nanorods.

In the recent years, by designing the surface of some materials at a subwavelength scale, new applications for optics were highlighted (see for example [33]). These new structures have been referred to as metasurfaces because they can modify the main physical characteristics of the incident light. These modifications include, the phase, the angular momentum, or the light polarization [34], and can generate and exalt nonlinear phenomena [35, 36, 37]. For example, plasmonic metasurfaces containing two-dimensional subwavelength gold patterns have been developed that allow imprinting arbitrary phase patterns onto a propagating beam [25] and perpendicular gold nanorods arrays have been used to perform polarization conversion control from the capacitive coupling to the conductive coupling regimes between the gold entities [34].

Metasurface physics also presents attractive opportunities for the thermoplasmonics. In particular, the design and the juxtaposition of elementary plasmonic cells sensitive to the incident polarization is a good manner to lead to efficient temperature

gradient controls. In figure (5), we consider a simple example of metasurface consisting of elementary cells containing four nanorods. In this paving, two consecutive plasmonic elements are perpendicular relative to each other, so that the excitation of the transverse and longitudinal modes will move from one structure to its neighbor, when progressively turning the polarization angle of the incident light. The next figure (6) displays the temperature map evolution expected around this metasurface geometry. These computations have been performed by keeping the same parameters as in the previous section, i.e., 16 cylindric gold nanorods (25×80 nm) illuminated in normal incidence by a linearly polarized plane wave (see geometry insert). The laser power S_0 is fixed at $5 \text{ mW}/\mu\text{m}^2$ and the lateral pitches, d_x and d_y between the rods are 250 nm. A detailed examination of the maps shows a regular shaping of the temperature distribution, in a range that varies from 5 degrees for an incident power of $5 \text{ mW}/\mu\text{m}^2$, and that displays a periodic series of hot spots with tunable location by applying a remote control of the polarization. For example, as shown in the first map of figure (6), a polarization parallel to OX axis yields a hot spot pattern distributed on a square lattice with a side equal to $\sqrt{2} \times$ the lateral nanorod pitch d_x . Consequently, by gradually turning the incident polarization, we can accurately drag these hot spots, in a controllable manner, from the parallel to perpendicularly oriented nanorods. In addition, as described in the *Supplemental Information Document* (see figures S2 and S3), such a local temperature gradient tuning leads to the possibility of controlling the heat flux in the vicinity of the metasurface.

This functionality is particularly attractive for nano-biology manipulations and applications, where tuning the symmetry of such temperature gradients would generate complex convection currents in liquids that could be advantageously exploited, for example, to thermally assisted plasmonic trapping [38, 39], to trigger thermotactic mobility or behavioral plasticity on demand [40, 41].

5. Evolutionary optimization of optical hybrid material meta-cells

In order to complete this theoretical paper, we demonstrate that our numerical technique is well-suited for the design of optimized thermoplasmonic meta-cells, using an evolutionary optimization (EO) algorithm. In the recent past, EO techniques have been successfully applied on various problems in nano-optics[42, 43, 44]. We will also use a multi-material structure in our demonstration, which means that each meta-cell (or meta-unit) is composed of multiple elements of different materials. Multi-material systems can be modeled with our approach by using position-dependent dielectric functions $\epsilon_p(\omega_0)$ in equation (22) for the meshpoints at \mathbf{r}_p . A full metasurface would finally consist of many of those optimized meta-units.

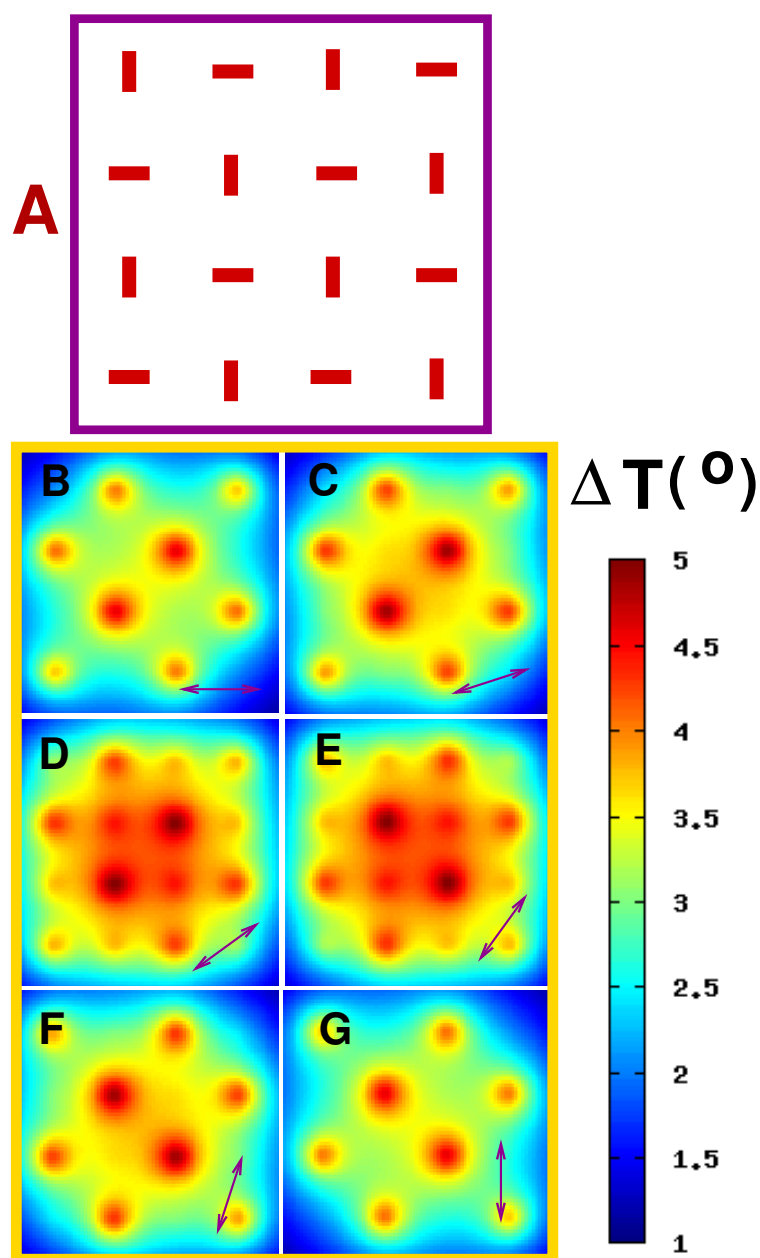


Figure 6. (color online) (A) Top view of the thermoplasmonic metasurface described in figure (5). (B) to (G) evolution of the temperature maps when the incident polarization, represented by a double red arrow, is turned from 0° to 90° with 18° steps.

5.1. Evolutionary optimization of photonic nano-structures

As illustrated in our previous examples (see section (4)), the design of geometric assemblies of nanostructures starts with the conception of a reference geometry by intuitive considerations. Via the systematic variation of a few parameters, this reference systems is then optimized within its possibilities. Such an approach, however, is limited to rather simple problems and requires a certain degree of understanding and intuition

for the considered system. In case of complex structures or complicated phenomena, the intuitive method often fails. To overcome these limitations, we apply in this section an evolutionary optimization algorithm in order to design a meta-unit for optimum nano-scale heat generation. EO is a heuristic optimization method to find the global maximum or minimum of complex, possibly non-analytic problems. EO algorithms use a *population* of parameter-sets for the problem, which are driven through a cycle of reproduction, evaluation and selection, in which weak solutions are iteratively eliminated and *strong* parameter-sets are kept. Here, we couple the “jDe” EO algorithm [45] provided by the “paGMO” toolkit [46] to our volume discretization method for full-field electro-dynamical simulations. For these simulations, we use our own toolkit “pyGDM” [47]. More details on the approach can be found in Ref. [44].

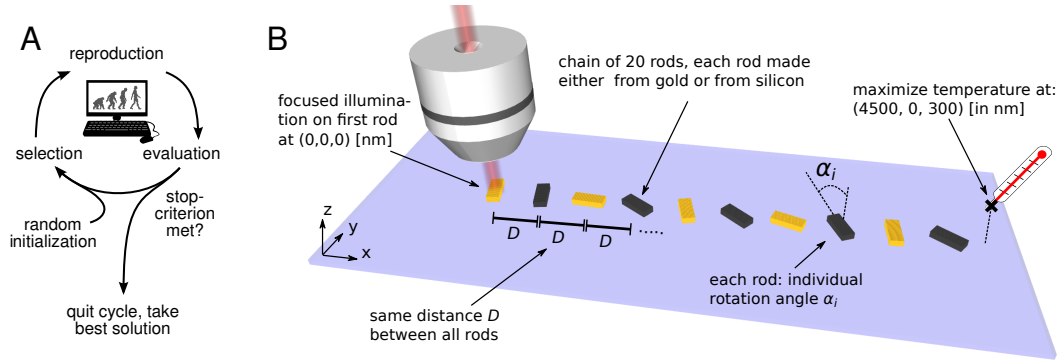


Figure 7. (color online) A) sketch of the evolutionary optimization scheme. (B) illustration of the optimization model and problem. A chain of 20 nano-rods on a glass substrate is searched in order to maximize the temperature increase at a specific location ($x = 4500, y = 0, z = 300$) [nm], far from the focal spot of a focused illumination (at $(x = 0, y = 0, z = 0)$ [nm]). The free parameters of the optimization are the angles α_i as well as the material (either gold or silicon) of each rod. As further parameter, the spacing D between the rods is optimized by the algorithm.

5.2. Optimization of a chain of nano-rods for localized heating

This problem is inspired by works which have shown that chains of both, dielectric and metallic nano-particles can effectively guide light along relatively large distances[49, 50]. Here, the aim of the optimization is to find a chain of 20 nano-rods (each rod of size $70 \times 175 \times 140 \text{ nm}^3$) which delivers the highest possible temperature increase at a specific location far from a focused illumination with a wavelength of $\lambda_0 = 600 \text{ nm}$. The focal spot with a beam waist of $w_0 = 300 \text{ nm}$ is set at the origin, centered on the first nano-rod (see also subplots (ii) in Fig. 8). The rods lie on a glass substrate ($n = 1.5, \kappa = 0.8 \text{ Wm}^{-1}\text{K}^{-1}$), in water ($n = 1.33, \kappa = 0.6 \text{ Wm}^{-1}\text{K}^{-1}$). The temperature increase ΔT is to be maximized at $(x = 4500, y = 0, z = 300)$ [nm]. The free parameters for the optimization are each rod’s rotation angle α_i , each rod’s material (either gold or silicon, refractive indices taken from Refs. [29, 48]) and the distance D between the nano-rods (which are equidistant along the chain). The geometry of the problem is depicted in

Fig. 7B. It is obvious, that a systematic evaluation of all possible solutions is impossible, considering the 41 free parameters. For the EO algorithm we use a population of 50 individuals, which we evolve for 2000 iterations. On an ordinary office PC (AMD FX-8350 CPU) one run never took longer than 24 hours. Figure 8 shows the results of the optimizations, the fitness as a function of the iteration number is shown in the subplots (i). In order to verify the convergence, we ran the optimizations several times with random initial parameters. The different runs yielded similar results, hence we conclude that the optimizations converged close to the global optimum.

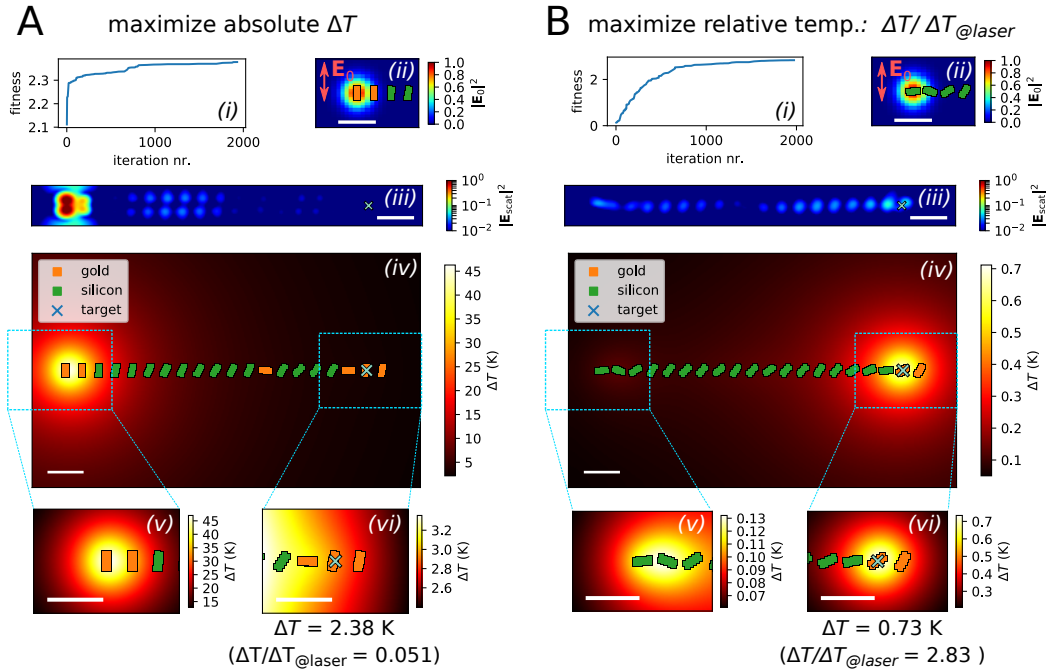


Figure 8. (color online) Results of the EO of a chain for a maximization of (A) the *absolute* temperature increase at the target location and (B) the *relative* temperature increase at the target position, normalized to $\Delta T_{@laser}$ at the location of the focused illumination. (i) convergence of the optimization. (ii) intensity of the incident field \mathbf{E}_0 , with focal spot of waist $w_0 = 300$ nm at $(0, 0, 0)$ nm, linearly polarized along OY ($\lambda_0 = 600$ nm). (iii) scattered field intensity on a logarithmic color scale, calculated 50nm above the chain of nano-rods (normalized to $|\mathbf{E}_0|^2$). (iv) mapping of the temperature increase along the chain. (v) and (vi) zooms around the focal spot and the location of the ΔT probe. All temperature mappings are calculated at a height of $z = 300$ nm. White scale bars are 500 nm. The optimization target location is indicated by a cross-shaped marker.

5.2.1. Maximize absolute temperature increase In the first run, the absolute temperature difference ΔT is the optimization target. The results are shown in figure 8A. The EO algorithm chose a spacing D of approximately 250nm. It placed two gold rods in the beginning of the chain, which are aligned with the incident light's polarization in order to obtain the strongest response and, consequently, the highest dissipation inside the metal. Following the first two gold blocks, a chain of silicon rods is guiding light

towards the target location, where further gold rods dissipate the arriving light into heat (see the scattered near-field in subplot (iii) of figure 8). The heat radiated from the two initial blocks locally rises the temperature by more than 45° . At $x = 4.5 \mu\text{m}$, the temperature still is increased by more than 2 degrees. The temperature rise is shown in subplots (iv)-(vi) of figure 8. The heat generation from the terminal gold elements in the chain is only contributing weakly to the total temperature increase, adding about 0.25° .

5.2.2. Maximize normalized temperature increase In a second run, the goal of the optimization is set to the *relative* temperature increase $\Delta T/\Delta T_{\text{laser}}$. We aim to maximize the temperature at the target location $(4500, 0, 300)$ [nm] normalized to the temperature at the position of the illumination beam at $(0, 0, 300)$ [nm]. The results of this simulation are shown in figure 8B. The spacing D was set by the EO again to approximately 250 nm, which seems to be ideal for guiding light through the chain at the illumination wavelength $\lambda_0 = 600$ nm. However, in contrast to the maximization of the absolute temperature, the EO algorithm chose silicon for the entire chain and placed two gold elements only at its very end. The first two nano-rods were furthermore rotated perpendicular to the light's polarization in order to minimize their optical response and hence reduce dissipation in the early chain. If the silicon-rod at $(0, 0, 0)$ were oriented along the polarization of \mathbf{E}_0 , it would induce a temperature increase of $\approx 1.4^\circ$ at $(0, 0, 300)$ [nm]. Despite their horizontal orientation, the first two silicon rods effectively couple light into the chain, through which it is guided towards the gold-rods at its end. There the light is dissipated inside the metal, which acts as a local heat source just below the target position. The solution, found by the EO, has a very low $\Delta T_{\text{laser}} \approx 0.13^\circ$ at the origin, but increases the temperature at the target location by $\Delta T \approx 0.73^\circ$. Compared to ΔT_{laser} , this is $\times 2.8$ higher.

6. Conclusion

To conclude, we have presented new geometries based on arrays of subwavelength metallic nanoparticles organized at the surface of a dielectric substrate that results in thermoplasmonic metasurfaces. The different kinds of arrays discussed here make possible an on-demand and spatially controlled rise of temperature by the mean of the incident wavelength and polarization. This approach, based on localized resonances, is complementary to high order plasmonic resonances in larger 2D cavities that allow for an all-optical and polarization dependent control of the temperature landscape in their vicinity [51]. The formalism used in this work is optimized for the direct space applications and provides convenient analytical formula, with which the mechanisms for converting light energy into heat can be intuitively represented for both spherical and elongated metallic particles. Using anisotropic polarizabilities, our approach reveals the clear relationship between excitation parameters (laser power, polarization, and wavelength) and expected thermal effects (heat amount, temperature, ...). Interestingly,

the extension of this formalism by means of a volume discretization procedure of the metallic structures placed in the vicinity of a solid–liquid interface, supplies a numerical test bench for future applications of complex metasurfaces in thermoplasmonics, such as those encountered in micro-fluidic environments for nano-biology. Finally, we demonstrated that evolutionary optimization together with nano-optical simulations allows finding geometric assemblies for complex thermoplasmonic problems. Using an appropriately formulated problem, a hybrid–material chain of silicon and gold nano-rods can be optimized such, that the optical energy, delivered by a focused illumination spot, is transferred towards a distant location where it is locally transformed into heat.

Acknowledgments: This work was supported by the Agence Nationale de la Recherche (ANR) (Grants ANR-13-BS10-0007-PlaCoRe), the Programme Investissements d’Avenir under the program ANR-11-IDEX-0002-02, reference ANR-10-LABX-0037-NEXT, and the computing center CALMIP in Toulouse.

- [1] W. L. Barnes, A. Dereux, and T. W. Ebbesen, *Nature* **424**, 824-830 (2003).
- [2] N. J. Halas, S. Lal, W.-S. Chang, S. Link, and P. Nordlander, *Chem. Rev.* **111**, 3913-3961 (2011).
- [3] A. G. Brolo, *Nature Photonics* **6**, 709 (2012).
- [4] H. Wei, Z. Wang, X. Tian, M. Kall, H. Xu, *Nat. Communications* **2**, 387 (2011).
- [5] S. Viarbitskaya, A. Teulle, R. Marty, J. Sharma, C. Girard, A. Arbouet, and E. Dujardin, *Nat. Materials* **12**, 426 (2013).
- [6] A. O. Govorov, W. Zhang, T. Skeini, H. H. Richardson, J. Lee, and N. A. Kotov, *Nanoscale Res. Lett.* **1**, 84 (2006).
- [7] A. O. Govorov and H. H. Richardson, *Nanotoday* **2**, 30 (2007).
- [8] H. H. Richardson, M. T. Carlson, P. J. Tandler, P. Hernandez, and A. O. Govorov, *NanoLetters*, **9**, 1139 (2009).
- [9] J. Chen, W.-K. Chen, J. Tang, and P. M. Rentzepis, *PNAS*, **108**, 18887 (2011).
- [10] H. Ma, P. M. Bendix, and L. B. Oddershede, *NanoLetters*, **12**, 3954 (2012).
- [11] G. Baffou and R. Quidant, *Laser Photonics Rev.* **7**, 171 (2013)
- [12] A. Cuche, A. Canaguier-Durand, E. Devaux, J. A. Hutchison, C. Genet, and T. W. Ebbesen, *NanoLetters*, **13**, 4230 (2013).
- [13] Z. J. Coppens, W. Li, D. G. Walker, and J. G. Valentine, *NanoLetters*, **13**, 1023 (2013).
- [14] B. Desiatov, I. Goykhman, and U. Levy, *NanoLetters*, **14**, 648 (2014).
- [15] J. B. Herzog, M. W. Knight, and D. Natelson *NanoLetters*, **14**, 499 (2014).
- [16] A. Sanchot, G. Baffou, R. Marty, A. Arbouet, R. Quidant, Ch. Girard, and E. Dujardin *ACS Nano*, **6**, 3434 (2012).
- [17] G. Baffou, R. Quidant, and Ch. Girard, *Appl. Phys. Lett.*, **94**, 153109 (2009).
- [18] G. Baffou, M. P. Kreuzer, F. Kulzer, and R. Quidant, *Optics Express*, **17**, 3291 (2009).
- [19] Ch. Girard, E. Dujardin, G. Baffou, and R. Quidant, *New Journal of Physics*, **10**, 105016 (2008).
- [20] M. Essone Mezeme and C Brosseau, *Phys. Rev. E* **87**, 012722 (2013).
- [21] G. Baffou, P. Berto, E. Bermudez Urena, R. Quidant, S. Monneret, J. Polleux, and H. Rigneault, *ACS Nano*, **7**, 6478 (2013).
- [22] A. Teulle, R. Marty, Ch. Girard, A. Arbouet, and E. Dujardin, *Opt. Communications*, **291**, 412 (2013).
- [23] S. J. Weber, G. Colas des Francs, and Ch. Girard, *Phys. Rev. B*, **91**, 205419 (2015).
- [24] C. Enkrich, M. Wegener, S. Linden, S. Burger, L. Zschiedrich, F. Schmidt, J. F. Zhou, Th. Koschny, and C. M. Soukoulis, *Phys. Rev. Lett.*, **95**, 203901 (2005).
- [25] N Yu, P. Genevet, M. A. Kats, F. Aieta, J-Ph. Tetienne, F. Capasso, Z. Gaburro, *Science*, **334**, 333 (2011).
- [26] N. Lawrence, J. Trevino, and L. Dal Negro, *Opt. Lett.* **37**, 5076 (2012).
- [27] J. N. Anker, W. P. Hall, O. Lyandres, N. C. Shah, J. Zhao, and R. P. Van Duyne, *Nat. Materials*, **7**, 442 (2008).
- [28] *Plasmonic Nanoparticle Networks*, Erik Dujardin and Christian Girard, “Handbook of Nanophysics” (K. Sattler, ed.), Taylor & Francis, London 2010, Chapter 27.
- [29] P. B. Johnson and R. W. Christy, *Phys. Rev. B* **6**, 4370 (1972).
- [30] S. Link, M. B. Mohamed, and M. A. El-Sayed, *J. Phys. Chem. B*, **103**, 3073 (1999).
- [31] L. D. Landau and E. M. Lifshitz, *Field theory*, Pergamon press, London, third edition (1960).
- [32] K. Metwally, S. Mensah, and G. Baffou, *ACS Photonics*, **4**, 1544 (2017).
- [33] N. Yu and F. Capasso, *Nat. Materials*, **13**, 139 (2014).
- [34] L.-J. Black, Y. Wang, C. H. de Groot, A. Arbouet, and O. L. Muskens, *ACS Nano*, **8**, 6390 (2014).
- [35] H. Linnenbank and S. Linden, *Optica*, **2**, 698 (2015).
- [36] A. E. Minovitch, A. E. Miroshnichenko, A. Y. Bykov, T. V. Murzina, D. N. Neshev, and Y. S.

- Kivshar, *Laser Photonics Rev.*, **9**, 195 (2015).
- [37] L.-J. Black, P. R. Wiecha, Y. Wang, C. H. de Groot, V. Paillard, Ch. Girard, O. L. Muskens, and A. Arbouet, *ACS Photonics*, **2**, 1592 (2015).
- [38] J. S. Donner, J. Morales-Dalmau, I. Alda, R. Marty, and R. Quidant, *ACS Photonics*, **2**, 355 (2015).
- [39] A. Cuche, O. Mahboub, E. Devaux, C. Genet, and T. W. Ebbesen, *Phys. Rev. Lett.*, **108**, 026801 (2012).
- [40] I. Mori and Y. Oshima, *Nature (London)* **376**, 344 (1995).
- [41] F. N. Hamada, M. Rosenzweig, K. Kang, S. R. Pulver, A. Ghezzi, T. J. Jegla, and P. A. Garrity, *Nature (London)* **454**, 217 (2008).
- [42] T. Feichtner, O. Selig, M. Kiunke, and B. Hecht, *Phys. Rev. Lett.*, **109**, 127701 (2012).
- [43] C. Forestiere, Y. He, R. Wang, R. Kirby, and L. Dal Negro, *ACS Photonics*, **3**, 68–78 (2016).
- [44] P. R. Wiecha, A. Arbouet, C. Girard, A. Lecestre, G. Larrieu, and V. Paillard, *Nature nanotechnology*, **12** (2), 163 (2017).
- [45] S. M. Islam, S. Das, S. Ghosh, S. Roy, and P. N. Suganthan, *IEEE Transactions on Systems, Man, and Cybernetics, Part B (Cybernetics)*, **42**, 482–500 (2012).
- [46] F. Biscani, D. Izzo, and C. H. Yam, arXiv:1004.3824 [cs, math], (2010).
- [47] P. R. Wiecha, arXiv:1802.04071 [cond-mat, physics:physics] (2018).
- [48] E. D. Palik, *Handbook of Optical Constants of Solids*, Academic Press, 547–569 (1997).
- [49] C. Girard and R. Quidant, *Optics Express*, **12**, 6141–6146 (2004).
- [50] R. M. Bakker, Y. F. Yu, R. Paniagua-Domínguez, B. Luk'yanchuk, and A. I. Kuznetsov, *Nano Letters*, **17**, 3458–3464 (2017).
- [51] P. Wiecha, M.-M. Mennemanteuil, D. Khlopin, J. Martin, A. Arbouet, D. Gérard, A. Bouhelier, J. Plain, and A. Cuche, *Phys. Rev. B* **96**, 035440 (2017).